



BNL-225692-2024-JAAM

SolventMediated Formation of Quasi2D DionJacobson Phases on 3D Perovskites for Inverted Solar Cells Over 23% Efficiency

S. Ramakrishnan, M. Cotlet

To be published in "Advanced Energy Materials"

September 2023

Center for Functional Nanomaterials
Brookhaven National Laboratory

U.S. Department of Energy

USDOE Office of Science (SC), Basic Energy Sciences (BES). Scientific User Facilities (SUF)

Notice: This manuscript has been authored by employees of Brookhaven Science Associates, LLC under Contract No. DE-SC0012704 with the U.S. Department of Energy. The publisher by accepting the manuscript for publication acknowledges that the United States Government retains a non-exclusive, paid-up, irrevocable, world-wide license to publish or reproduce the published form of this manuscript, or allow others to do so, for United States Government purposes.

DISCLAIMER

This report was prepared as an account of work sponsored by an agency of the United States Government. Neither the United States Government nor any agency thereof, nor any of their employees, nor any of their contractors, subcontractors, or their employees, makes any warranty, express or implied, or assumes any legal liability or responsibility for the accuracy, completeness, or any third party's use or the results of such use of any information, apparatus, product, or process disclosed, or represents that its use would not infringe privately owned rights. Reference herein to any specific commercial product, process, or service by trade name, trademark, manufacturer, or otherwise, does not necessarily constitute or imply its endorsement, recommendation, or favoring by the United States Government or any agency thereof or its contractors or subcontractors. The views and opinions of authors expressed herein do not necessarily state or reflect those of the United States Government or any agency thereof.

Solvent-Mediated Formation of Quasi-2D Dion-Jacobson Phases on 3D Perovskites for Inverted Solar Cells over 23% Efficiency

*Shripathi Ramakrishnan, Donghoon Song, Yuanze Xu, Xiaoyu Zhang, Gavin Aksoy, Mircea Cotlet, Mingxing Li, Yugang Zhang, and Qiuming Yu**

S. Ramakrishnan, D. Song, Y. Xu, X. Zhang, G. Aksoy, Q. Yu

Robert Frederick Smith School of Chemical and Biomolecular Engineering

Cornell University

Ithaca, NY 14853, USA

Email: qy10@cornell.edu

M. Cotlet, M. Li, Y. Zhang

Centre for Functional Nanomaterials

Brookhaven National Laboratory

Upton, NY 11973-5000, USA

Abstract

1 2D-on-3D (2D/3D) perovskite heterostructures present a promising strategy to
2 realise efficient and stable photovoltaics. However, their applicability in inverted solar
3 cells is limited due to the quantum confinement of the 2D-layer and solvent
4 incompatibilities that disrupt the underlying 3D layer, hampering electron transport at
5 the 2D/3D interface. Herein, we investigate solvent-dependent formation dynamics
6 and structural evolution of 2D/3D heterostructures via *in-situ* X-ray scattering. We
7 reveal that solvent interaction with the 3D surface determines the formation sequence
8 and spatial distribution of quasi-2D phases with $n = 2-4$. Isopropanol (IPA) reconstructs
9 the perovskite into a PbI_2 -rich surface, forming a strata with smaller n first, followed by
10 a thinner substratum of larger n . In contrast, 2,2,2-Trifluoroethanol (TFE) preserves
11 the 3D surface, promoting the formation of uniformly distributed larger n domains first,
12 and smaller n last. Leveraging these insights, we use Dion-Jacobson perovskites with
13 superior charge transport properties and structural robustness to fabricate 2D/3D
14 heterostructures dominated by $n \geq 3$ and engineer a favourable energy landscape for
15 electron tunnelling. Proof-of-concept inverted solar cells based on 3-
16 Aminomethylpyridine and TFE achieve a champion efficiency of 23.60%, with V_{oc} and
17 FF of 1.19 V and 84.5%, respectively, and superior stabilities with t_{94} of 960 h under
18 thermal stress.

19

20

21

22

23

24

25

26

27

28

29

30

31

32

33

34

35

36

37

38

39

40

41

42

43

44

45

46

47

48

49

50

51

52

53

54

55

56

57

58

59

60

61

62

63

64

65

1. Introduction

2 Two-dimensional metal-halide perovskites (2D-MHPs) have emerged as a new
3 family of photovoltaic materials proven to resolve the extrinsic stability in
4 perovskites.^[1,2] Typically, 2D-MHP frameworks are composed of n layers of corner-
5 sharing $[\text{BX}_6]^{4-}$ octahedral frameworks sandwiched between two layers of bulky
6 organic ligands.^[3,4] Among these, two prominent 2D-MHP classes observed and
7 characterised include the Ruddlesden-Popper perovskite (RPP) phase $\text{A}'_2(\text{A})_{n-1}\text{B}_n\text{X}_{3n+1}$ and the Dion-Jacobson perovskite (DJP) phase $\text{A}''(\text{A})_{n-1}\text{B}_n\text{X}_{3n+1}$, where A' and
8 A'' are bulky organic mono- and diammonium ligands, respectively.^[5] However, the
9 coexistence of high efficiency and long-term stability has become a crucial
10 requirement for the application of perovskite solar cells (PSCs). While 2D-MHP films
11 with $n \geq 4$ exhibit excellent operational stabilities,^[6-8] the power conversion efficiencies
12 (PCEs) of the resulting devices significantly fall behind their three-dimensional
13 counterparts (3D-MHPs).^[9-11]

14 To date, the most promising strategy to leverage the structural integrity of 2D-
15 MHPs with the superior carrier dynamics of 3D-MHPs involves the formation of 2D-
16 on-3D (2D/3D) heterostructures.^[12,13] Typically, a layer of ligand salts is deposited atop
17 a 3D-MHP, leading to the formation of $n = 1$ or 2 2D-MHP phases on the 3D-MHP
18 surface, passivating surface traps and facilitating electron-blocking^[14], significantly
19 improving the open-circuit voltage V_{oc} and fill factor FF of arising solar cells.^[15]
20 However, this strategy has invoked mixed results for the commercially relevant p-i-n
21 structured PSCs, where photogenerated electrons and holes in perovskites are
22 collected by the top metal cathode and the bottom transparent conductive oxide
23 anode, respectively.^[16] The quantum-confinement effect imposed by the bulky ligands
24 leads to shallower conduction band minima in 2D-MHPs compared to 3D-MHPs. As a
25 result, the arising 2D/3D heterostructures exhibit electron blocking, which is
26 detrimental to electron collection in p-i-n PSCs. Gharibzadeh et al. reported the use of
27 phenylethylammonium chloride (PEACl) for dual passivation of grain boundaries and
28 perovskite surface to form mixed domains of $n = 1$ and 2 RPP phases to achieve a
29 high V_{oc} of 1.16 V on p-i-n PSCs.^[17] More recently, Huang et al. regulated the rate of
30 cation exchange during 2D/3D heterostructure formation via a diamine masking
31 reagent on a 3D-MHP surface, followed by subsequent 2D-MHP formation ($n = 1$ and
32 2 with PEABr) to achieve excellent PCEs of 24.7% with an exceptional V_{oc} of 1.20
33 V.^[18]

V.^[18] In contrast, La-Placa and Sidhik et al. report inferior device performance arising from misaligned energy levels among the conduction band minimum (CBM) of 2D- and 3D-MHP and the lowest unoccupied molecular orbital (LUMO) of the electron transport layer (ETL), with significant electron blocking by the phase-pure 2D-overlayers up to $n = 3$, even for low capping thicknesses below 8 nm.^[19,20] Thus, weakening the degree of quantum-confinement of the 2D-MHP layers and fine-tuning the energy alignment at the 3D/2D/ETL interfaces to allow electron tunnelling to the ETL remains a longstanding issue.

The degree of quantum-confinement may be reduced by manipulating the number of octahedral layers n because the energy landscape of 2D-MHPs is significantly narrowed for larger n values ($n = 3$ and 4).^[1,3,21] A majority of previous research has focussed on identifying specific ligands to form suitably larger n fragments by tuning the reactivity, steric hinderance, and atomic radius of the ligand in conjunction with suitable post-treatment.^[22–25] More critically, Chen et al. reveal rational solvent selection as the key to manipulating 2D-MHP distribution through the inclusion of excess methylammonium iodide (MAI) and dimethylformamide (DMF) in the ligand solution to generate greater density of MA^+ and PbI_2 , indeed paving the way for tuning n of 2D-MHPs in p-i-n solar cells. As such, the ligand species used and the solvent properties (e.g., polarity and interaction with 3D-MHP) decide the arising phase-formation behaviour.^[26] However, most of these works employ solvents that irrevocably damage the 3D-MHP surface (e.g., isopropanol (IPA)) as the ligand processing solvent of choice. Recently, it was revealed that IPA reconstructs the 3D-MHP surface into a relatively more PbI_2 -rich state during post-treatment.^[27] The shallow iodide defects thus formed lower the activation barrier for perovskite transformation into a non-photoactive phase.^[28] Therefore, it is necessary to expand the library of processing solvents with a view of understanding the solvent interaction on the 3D-MHP surface termination to favourably drive the growth of larger n 2D-MHPs.

Furthermore, most recent works are limited to the RPP analogue of 2D-MHPs, which feature highly anisotropic charge carrier transport with charge carrier mobilities across the bulky organic ligands (out-of-plane) being magnitudes smaller than the in-plane counterpart along the $[\text{PbX}_6]^{4-}$ framework.^[29] RPPs are also characterised by a Van der Waal gap between ligands, with a substantial charge tunnelling barrier across adjacent $[\text{PbX}_6]^{4-}$ frameworks ($> 10 \text{ \AA}$).^[5,30] These shortcomings are accentuated by

1 the tendency of 2D-MHPs to adopt a horizontal or mixed orientation on top of the 3D-
2 MHPs.^[18] DJP_s, as a less investigated structural analogue of 2D-MHPs, offer
3 possibilities to diminish the effect of quantum-confinement.^[31] The diammonium
4 ligands templating DJP_s bring the adjacent $[PbX_6]^{4-}$ frameworks closer, well within the
5 range of charge tunnelling through the insulating ligands (c.a. 4 Å), and facilitating
6 relatively more symmetric charge transport.^[32]
7
8

9 In this paper, we investigate the formation mechanisms of 2D DJP on 3D-MHP
10 heterostructures. We find that the formation dynamics and n of 2D-MHP capping
11 layers are inextricably tied to the solvent-induced surface reconstruction of the
12 underlying 3D-MHP. Isopropanol (IPA) reconstructs the 3D-MHP surface into a PbI_2 -
13 rich state, while 2, 2, 2-trifluoroethanol (TFE) inflicts almost no damage, preserving
14 the FA/MA-rich surface. *In-situ* GIWAXS reveals that 2D/3D formation with IPA-based
15 solvent mixtures proceeds via the initial formation of a smaller n strata, followed by a
16 sparse substratum of larger n , while TFE leads to nucleation of larger n first and
17 smaller n last, uniformly distributed across the 2D-MHP cross-section. In addition, the
18 abundance of nucleation sites created during surface reconstruction by IPA presents
19 a diffusion barrier for 2D-MHP formation, severely hindering the growth of larger n ,
20 while fewer nucleation sites during TFE treatment allows uniform ligand distribution,
21 leading to 2D-MHP growth dominated by $n \geq 3$. Based on these insights, we fabricated
22 2D/3D heterostructures based on RPP and DJP capping layers via synergistic solvent
23 and ligand engineering to tailor the energy landscape of p-i-n solar cells. Proof-of-
24 concept 2D/3D films dominated by $n \geq 3$ based on 3-aminomethylpyridinium diiodide
25 (3-AMPY) DJP_s exhibit very long electron diffusion lengths up to 4 μm compared to
26 their RPP analogues. Simultaneously, the DJP_s enable favourable CBM alignment at
27 the 3D/2D/ETL interfaces, with significantly reduced quantum-confinement and barrier
28 to electron transport. Inverted 2D/3D PSCs based on 3-AMPY and TFE-based
29 solvents achieve a champion power conversion efficiency of 23.60% with a
30 remarkable V_{oc} and FF of 1.19 V and 84.5%, respectively. Furthermore, the defect-
31 free capping layers produced via TFE treatment benefit from the favourable energy
32 landscape, strong electrostatic bonding and structural integrity of DJP_s to achieve
33 superior stabilities with t_{92} of 1440 h under ambient conditions (RH = 50-60%) and t_{94}
34 of 960 h at 85°C.
35
36
37
38
39
40
41
42
43
44
45
46
47
48
49
50
51
52
53
54
55
56
57
58
59
60
61
62
63
64
65

1 2. Results and Discussion

3 2.1. Ligand effect on the energy landscape of 2D-MHPs

4
5
6
7
8
9
10
11
12
13
14
15
16
17
18
19
20
21
22
23
24
25
26
27
28
29
30
31
32
33
34
35
36
37
38
39
40
41
42
43
44
45
46
47
48
49
50
51
52
53
54
55
56
57
58
59
60
61
62
63
64
65
The major hurdle towards the development of 2D/3D p-i-n PSCs lies in the upshifted CBM of the quantum-confined 2D-MHP capping layer. A 2D-MHP capping layer with $n > 2$ phases with reduced quantum-confinement should be beneficial to PCE via simultaneous defect passivation and improved charge carrier transport. The quantum-confinement may also be modulated by rational bulky organic ligand selection. **Figure 1a** displays representative RPP and DJP phases, where RPPs have two layers of interdigitating ligands held by weak Van der Waal forces, while DJPs have a single layer of ligands separating the inorganic octahedral frameworks. The ligands influence the crystal configuration and interlayer spacing of inorganic octahedral frameworks on many levels, depending on the charge, functional group position, and steric effects.^[33] These parameters, particularly the octahedral distortion and framework-to-framework interlayer spacing, should have a profound impact on the electronic structure.^[33] Accordingly, the DJP-forming ligands 3-aminomethylpyridine (3-AMPY) and 4-aminomethylpyridine (4-AMPY) were shortlisted as possible ligands for 2D-MHP capping layer due to their narrow interlayer spacing and lower octahedral distortion versus RPP-forming phenylethylamine PEA (Figure 1b).

36
37
38
39
40
41
42
43
44
45
46
47
48
49
50
51
52
53
54
55
56
57
58
59
60
61
62
63
64
65
To visualise their band structure with respect to 3D-MHPs, we performed ultraviolet photoelectron spectroscopy (UPS) on thin films of RPP and DJP with PEA and 3-AMPY as ligands, respectively (Figure 1c). Thin films were fabricated by first preparing single crystals of phase-pure $n = 3$ $(\text{PEA})_2\text{MA}_2\text{Pb}_3\text{I}_{10}$ and $(3\text{-AMPY})\text{MA}_2\text{Pb}_3\text{I}_{10}$ and translating their purity into thin-films. (Refer to Supplementary Note 1 and Figure S1). As expected of quantum-confined structures, the valence band maximum (VBM) and CBM are noticeably offset from those of the 3D-MHP. A shorter halide-halide interlayer distance should lead to a greater degree of antibonding, pushing up the VBM. Accordingly, the VBM of the 3-AMPY 2D DJP film is shifted upwards by c.a. 0.03 eV compared to the PEA RPP film. Estimating the CBM position using the optical bandgap (2.03 eV for PEA and 1.93 eV for 3-AMPY, Figure S1b) yielded CBM values of -3.75 and -3.82 eV for $n = 3$ PEA and 3-AMPY 2D-MHP films, respectively. The downshifted CBM of 3-AMPY DJP is consistent with the reduced octahedral distortion of $n = 3$ 3-AMPY DJP.^[31] A reduced octahedral distortion can

provide new hybrid orbitals via *s* and *p* halide orbital hybridisation, pushing down the CBM.^[34] While the reduced CBM of 3-AMPY DJP certainly displays a noticeable offset compared to the 3D-MHP, the smaller degree of CBM offset and shorter interlayer distance should benefit electron tunnelling compared to the RPP analogue. A thin capping layer (c.a. 10-20 nm) dominated by $n \geq 3$ DJPs should take advantage of both factors to realise efficient p-i-n PSCs.

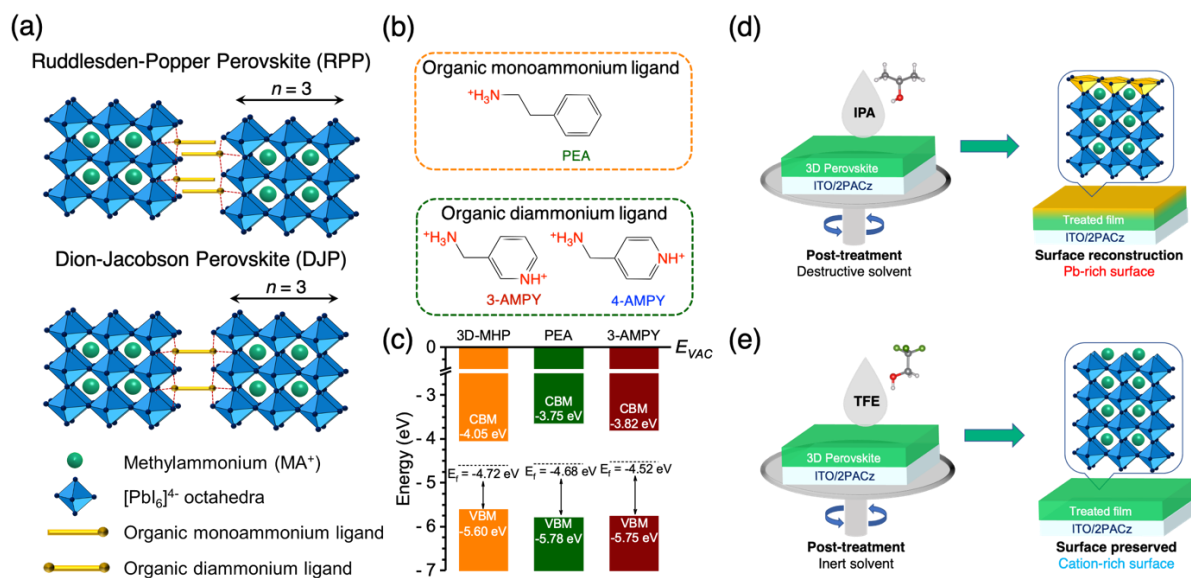


Figure 1. (a) Schematic representation of $n = 3$ 2D RPP and DJP. (b) The three ligands used to prepare 2D/3D heterostructures in this study: RPP-forming PEA and DJP-forming 3-AMPY and 4-AMPY. (c) The UPS measured band levels of representative 3D-MHP and $n = 3$ 2D RPP and DJP illustrating the effect of reducing quantum confinement via forming 2D DJP on the CBM. (d-e) Schematics representing the impact of destructive IPA solvent and inert TFE solvent on 3D-MHP surface.

2.2. Solvent-mediated 3D-MHP surface reconstruction

To leverage the reduced electron transport barrier of DJPs towards efficient p-i-n PSCs, we sought to design surface treatments driven towards the preferential formation $n \geq 3$ phases atop a 3D template. One of the critical considerations towards the phase formation tendency of 2D/3D-MHPs lies in the surface composition prior to 2D-MHP formation, which is inextricably linked to the interaction between perovskite and the ligand processing solvent.^[18,24,27] Conventionally, most studies have employed isopropanol (IPA) to great effect due to its ability to dissolve a broad window of ligands.^[12,26] However, IPA tends to leach off small organic cations (MA^+ , FA^+) to reconstruct the 3D-MHP surface into a relatively PbI_2 -rich state (Figure 1d) during

1 post-treatment, with a very unstable and reactive surface.^[27] The PbI_2 -terminated
2 surface has a heightened binding affinity for 2D-MHP forming ligands, leading to a
3 rapid and uncontrolled reaction almost ubiquitously forming $n = 1$ and 2 in the
4 majority.^[27,35] Furthermore, the post-treated surface tends to possess FA/MA-
5 vacancies, which generate defects and facilitate 3D-MHP degradation.^[28] On the other
6 hand, solvents with weak interaction with 3D-MHPs (e.g., chloroform (CF)) allow
7 ligand deposition onto an intact 3D-MHP surface (Figure 1e).^[36] The spontaneous
8 cation exchange between deposited ligands and FA^+/MA^+ that constitute the surface
9 termination^[27,37] leads to progressive dimensional reduction by initially forming larger
10 n intermediates (from $n = 3 \rightarrow 2 \rightarrow 1$).^[38] Thus, we hypothesise that regulating the
11 surface composition by tuning solvent interaction with 3D-MHP and interrupting the
12 dimensional reduction should afford large n . However, the applicability of CF is
13 severely hindered by the solubility window being limited to predominantly long aliphatic
14 ammonium salts.^[34] Thus, we turned to screen alternative solvent combinations that
15 have a weak affinity for 3D-MHP surface while still dissolving 3-AMPY and 4-AMPY
16 ligands to fabricate the desired DJP/3D-MHP heterostructures with large n .
17

18 Fluorinated solvents possess a weaker solvation effect than their non-
19 fluorinated counterparts. In particular, 2, 2, 2-trifluoroethanol (TFE) is a protic solvent
20 with very strong hydrogen bond donating ability but weaker electron pair donation due
21 to the highly electronegative $-\text{CF}_3$ group (Figure 1e). Consequently, TFE has a strong
22 solvation effect on anions, while weakly solvating cations. Thus, we anticipated that
23 TFE as a ligand solvent would lead to less pronounced surface reconstruction and low
24 FA^+/MA^+ leaching while still possessing sufficient polarity and dielectric constant
25 necessary to dissolve the ligands salts in Figure 1b. As TFE is a more polar solvent
26 than IPA, the penetration by the solvent into the 3D-MHP film should be greater,
27 allowing a more uniform distribution of ligands into the 3D-MHP grain boundaries.
28 Thus, we investigated the 3D-MHP surface reconstruction effect of triple-cation
29 $\text{Cs}_{0.03}(\text{FA}_{0.90}\text{MA}_{0.10})_{0.97}\text{PbI}_3$ 3D-MHP films exposed to neat IPA and TFE by analysing
30 the carrier lifetime and spectral properties using time-resolved photoluminescence
31 (TRPL) and static photoluminescence (PL). Films subjected to a brief exposure to IPA
32 exhibit slightly lower carrier lifetimes and PL intensity compared to pristine while TFE-
33 exposed films remain almost no changes (Figure S3). Additionally, to mimic scaled-
34 up fabrication conditions, we immersed 3D-MHPs in IPA and TFE for a period of 24 h.
35 Ostensibly, the 3D-MHP immersed in IPA forms a golden-yellow film surface,
36

1 indicating the formation of a PbI_2 or $\delta\text{-FAPbI}_3$ -rich surface with pronounced surface
2 reconstruction. In contrast, the TFE-immersed film displays very little change in
3 appearance (Figure S4).

4 We included a trace quantity of polar, coordinating solvent (DMF) to generate
5 free octahedra and allow deeper penetration of ligands into the 3D-MHP.^[26] To
6 evaluate the leaching capability of solvent mixtures with 0.5 vol% of DMF, we spin-
7 coated 100 μL neat IPA:DMF and TFE:DMF onto a 3D-MHP film. Scanning Electron
8 Microscopy (SEM) revealed that the surface of the 3D-MHP was completely
9 reconstructed into bright platelets, which are likely PbI_2 crystallites^[39], with significant
10 phase segregation upon IPA:DMF washing (Figure S5b). However, the morphology of
11 the pristine film and TFE:DMF-treated film are comparable, indicating minimum
12 structural damage (Figures S5a and c). In addition, we studied the PL distribution
13 across the film surface using confocal photoluminescence mapping (CPLM). Figure
14 S6a exhibits the CPLM of a typical 3D-MHP, with alternating bright domains at the
15 centre of a single grain and dark domains at the grain boundaries. In contrast, the
16 overall PL intensity of IPA:DMF washed films is bleached tremendously, characteristic
17 of a defect-riddled surface with significant non-radiative recombination (Figure S6b).
18 TFE:DMF washing, on the other hand, elicits comparable emission characteristics to
19 the pristine 3D-MHP (Figure S6c). Lastly, the X-ray diffraction patterns collected from
20 the three representative films exhibit a noticeable PbI_2 peak in the case of IPA:DMF
21 treated film compared to the TFE:DMF washed and pristine 3D-MHP film (Figure S7).
22 Overall, the results collectively report the destructive nature of the IPA:DMF mixture
23 by generating a relatively PbI_2 -rich surface and the relatively inert nature of the
24 TFE:DMF mixture towards maintaining a relatively unharmed FA^+/MA^+ -rich 3D-MHP
25 surface. The above dichotomy in the surface types manifests remarkable differences
26 during 2D-MHP formation.

2.3. *In-situ* GIWAXS of 2D-MHP formation during spin-coating and annealing

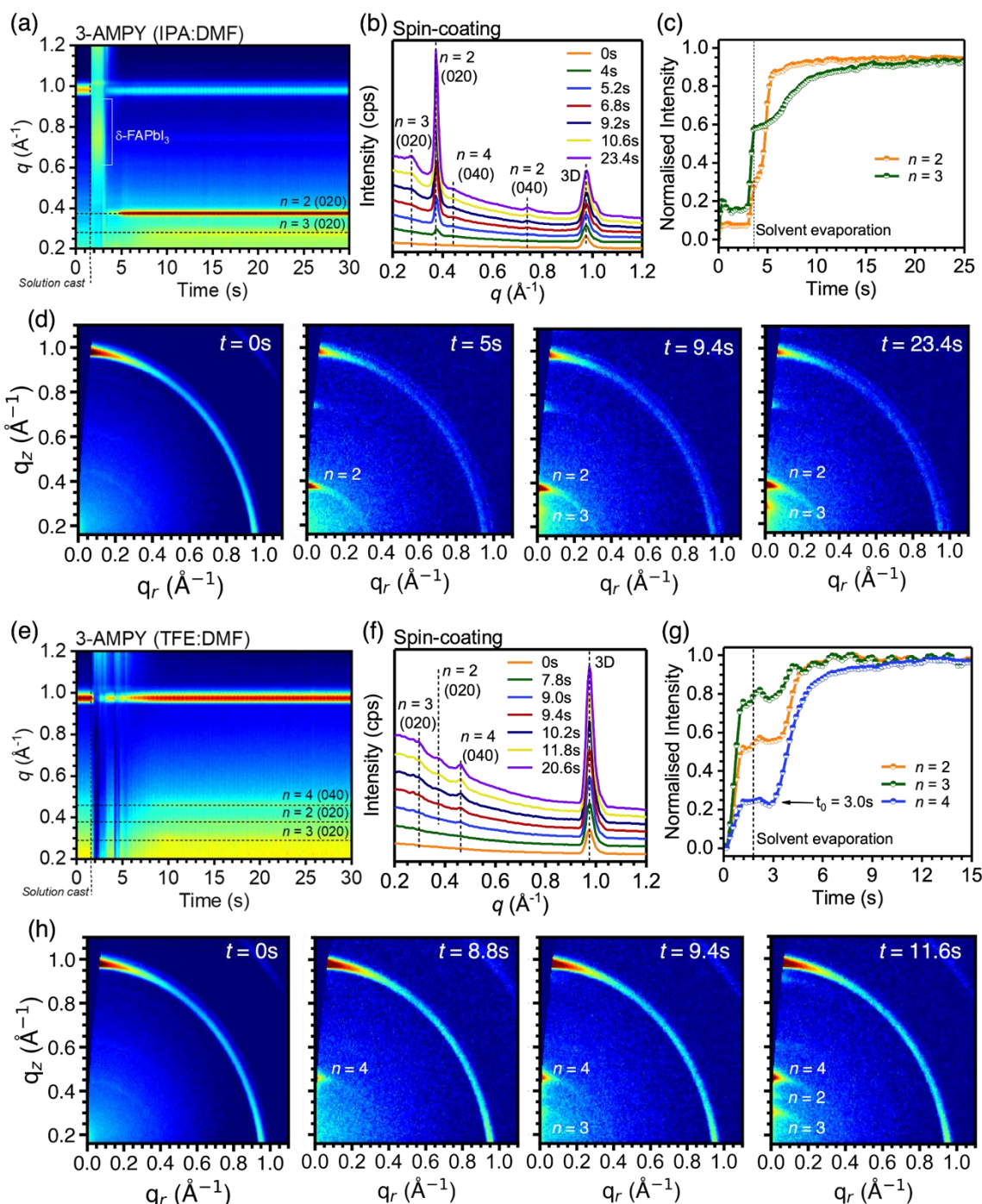


Figure 2. (a), (e) Azimuthally-integrated *in-situ* GIWAXS heat map during spin-coating, (b), (f) circularly-averaged linecuts, (c), (g) the temporal evolution of relevant 2D-MHP peaks, (d) and (h) individual GIWAXS heat maps at representative timestamps for as-spun films of 2D/3D films post-treated using 3-AMPY + MAI (2 mg/mL each) in IPA:DMF (a-e) and TFE:DMF (f-i), respectively. A grazing-incidence angle of 0.15° was maintained throughout the *in-situ* GIWAXS experiment.

We employed *in-situ* GIWAXS measurements to derive insights into the influence of solvent mixture on the film evolution of 2D/3D heterostructures. To achieve this, we spun a glass/Cs_{0.03}(FA_{0.90}MA_{0.10})_{0.97}PbI₃ 3D-MHP film at 2000 rpm and discharged a ligand solution (2 mg/mL 3-AMPY, 2 mg/mL of MAI and 0.5 vol% DMF in IPA or TFE) at c.a. 1.6 s (Figure S8). We emphasise that MAI was introduced to all ligand solutions in this work to allow larger n formation unless explicitly stated. For brevity, the solutions and 2D/3D heterostructures fabricated using 3-AMPY as the bulky organic ligand and IPA:DMF or TFE:DMF as the ligand solution will be dubbed 3-AMPY (IPA:DMF) and 3-AMPY (TFE:DMF) **and vice versa**.

Heatmaps of azimuthally integrated *in-situ* GIWAXS patterns, circularly-averaged linecuts, **intensity of relevant DJP peaks over time and representative GIWAXS timestamps** are displayed in **Figures 2a-d and e-h**, for 3-AMPY (IPA:DMF) and 3-AMPY (TFE:DMF), respectively. Before the discharge of ligand solution, a strong peak prevails at 0.97 Å⁻¹ (Figures 2a, **e**), corresponding to 3D-MHP. When IPA:DMF is employed in ligand solution, two broad halos are observed at 0.80 and 1.43 Å⁻¹ along the q_z -axis immediately upon solvent exposure (Figures 2a, S9a), corresponding to δ-FAPbI₃ and isopropanol solvent, respectively. ^[27,35] Typically, δ-FAPbI₃ was formed in systems when 3D-MHPs are dipped into IPA baths containing FAI or ligands, precluding the degradation of 3D-MHP into PbI₂. Immediately after solvent evaporation (3.6 s), the 3D-MHP peak displays a pronounced drop in intensity, **implying surface reconstruction of the 3D-MHP**. **Figures 2a, c and d** show that after complete solvent drying, scattering peaks appear at $q = 0.38$ Å⁻¹ ($d \approx 16.52$ Å) at an initial time scale at ~4 s, corresponding to $n = 2$ (3-AMPY)MAPb₂I₇ phase. After a substantial delay of ~5 s, a weaker peak corresponding $n = 3$ ($q = 0.28$ Å⁻¹, $d \approx 22.35$ Å) appears (Figure 2a, c). ^[31] **Thus, $n = 3$ formation only occurs after the termination of the $n = 2$ DJP**. A peak at $q = 0.45$ Å⁻¹ ($d \approx 14$ Å) that grows concurrently with $n = 3$ also appears, corresponding to the (040) diffraction of $n = 4$ (Supplementary Note 2). The GIWAXS timestamps during spin coating in Figure 2d show that all diffraction peaks of 2D-MHPs are strongly centred at $q_x = 0$ Å⁻¹, implying that the DJPs thus formed adopt a parallel orientation to the glass substrate. It is noteworthy that supplementing MAI in the ligand solution has led to total suppression of $n = 1$ (3-AMPY)PbI₄ phase. Indeed we note the formation of the corresponding $n = 1$ or $n > 2$ phase for 2D/3D heterostructures fabricated using a ligand solution composed of 3-AMPY and IPA:DMF without MAI or DMF, respectively (**Figures S11b and c**).

The *in-situ* GIWAXS revealed striking differences when processed using TFE:DMF, as displayed in Figures 2f-h. Immediately upon ligand solution discharge, we observed only a single halo centred at the q_z -axis at 1.42 \AA^{-1} ($d = 4.42 \text{ \AA}^{-1}$) representing TFE solvent (Figure S9b), again reiterating that TFE-based solvents do not reconstruct the 3D-MHP surface. Figures 2e-h show that at ~ 8 s, faint scattering peaks centred at $q_x = 0 \text{ \AA}^{-1}$ come to the fore at $q = 0.45 \text{ \AA}^{-1}$, corresponding to (040) diffraction of $n = 4$ (3-AMPY)MA₃Pb₄I₁₃ phase, with $n = 3$ phase in close succession at $q = 0.28 \text{ \AA}^{-1}$ (Figure 2g). Similar to IPA:DMF, the GIWAXS timestamps (Figure 2h) reveal that the DJPs adopt a parallel orientation with respect to the substrate. The peak corresponding to the $n = 2$ phase appears 0.8 s later. While the onset for crystallisation is slower in the case of TFE:DMF solvent as compared to IPA:DMF, the sequential appearance of different n phases is considerably faster. Furthermore, in stark contrast to the IPA:DMF sample where 2D-MHP formation progressed via $n = 2 \rightarrow 3 \approx 4$ formation, TFE:DMF-treated samples exhibit the opposite trend with $n = 4 \rightarrow 3 \rightarrow 2$. Contrastingly, Sargent et al. report the dimensional reduction from an initially $n = 3$ rich state to a final pure $n = 1$ state via interconversion of 2D-MHP phases for a VBABr-based RP 2D/3D heterostructures processed from an inert solvent CF:IPA (97:3 v/v).^[38] As Dion-Jacobson analogues possess stronger electrostatic bonds and a rigid lattice, they are more resilient to subsequent bifurcation/growth by 3-AMPY or MAI intercalation.^[40]

We explain the trends and sequence of 2D-MHP formation through isothermal classical Avrami analysis (Figure S12).^[41-44] IPA:DMF samples display an interface-limited crystallisation pathway during the early stage formation of $n = 2$ DJPs, followed by the diffusion-limited formation of $n = 3$ DJPs (Figure S12a). Based on the IPA:DMF-induced surface reconstruction, we reasoned that during post-treatment, a large number of nucleation sites (PbI₂) are formed on the 3D-MHP surface. Thus, the rate limiting steps to 2D-MHP formation were the initial physisorption of ligands or MAI to the 3D-MHP surface, rapidly forming $n = 2$ and the subsequently limited diffusivity of ligands across the solid bulk of the $n = 2$ DJP (Figure S12a and Supplementary Note 3). In contrast, TFE:DMF solvents do not leach the surface cations, presenting very few nucleation sites for the ligands, causing site-saturation (Figure S12b, Supplementary Note 3). As a result, ligand physisorption is limited in comparison, leading to a more uniform ligand distribution across both the 3D-MHP surface and

1
2
3
4
5
6
7
8
9
10
11
12
13
14
15
16
17
18
19
20
21
22
23
24
25
26
27
28
29
30
31
32
33
34
35
36
37
38
39
40
41
42
43
44
45
46
47
48
49
50
51
52
53
54
55
56
57
58
59
60
61
62
63
64
65

grain boundaries, causing nearly simultaneous formation of large n DJPs as seen in Figure 2e.

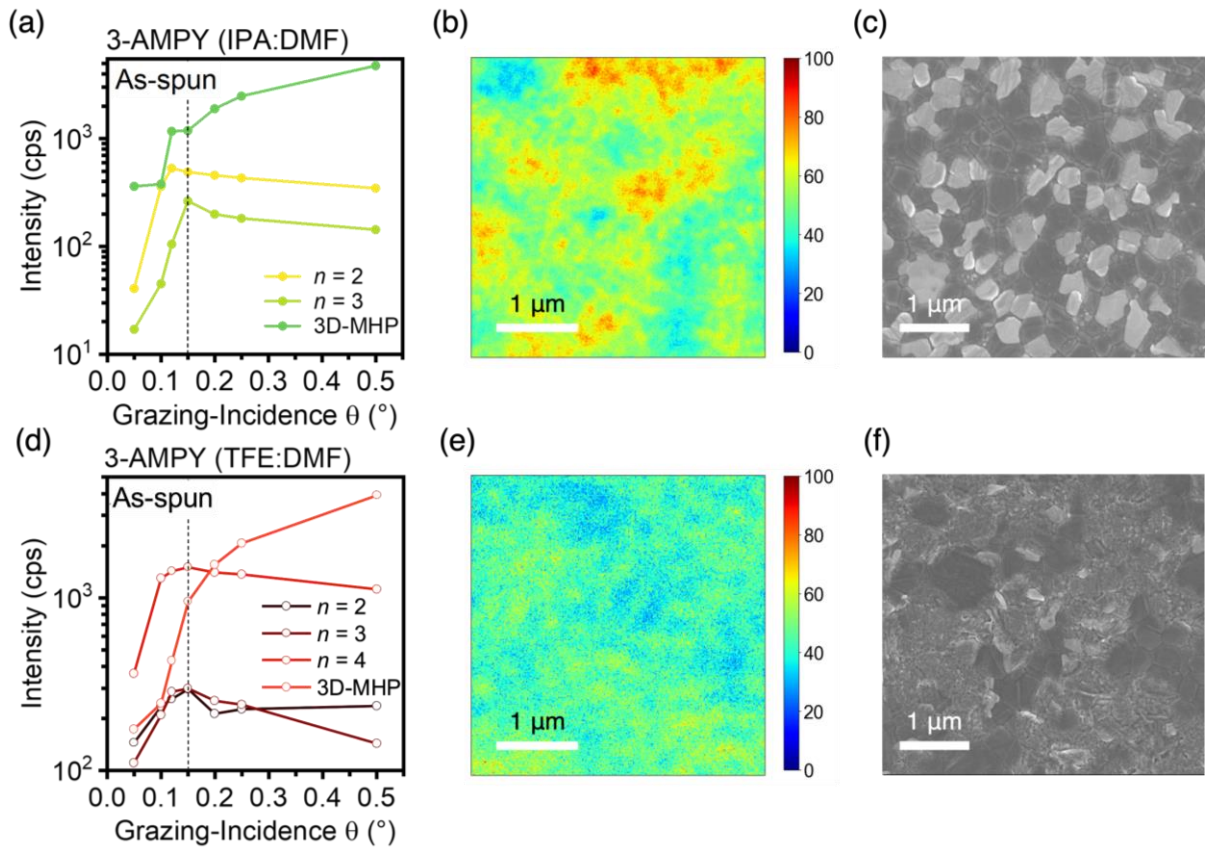


Figure 3. (a), (d) *Ex-situ* GIWAXS intensity of 2D-MHPs and 3D-MHP extracted via area-integrated peaks of n as a function of grazing-incidence angle with the critical angle (0.15°) marked as a dashed line, (b), (e) confocal photoluminescence mapping (CPLM) with 400 nm excitation and a 700 nm short-pass filter and (c), (f) topological SEM images of as-spun 3-AMPY (IPA:DMF) (a-c) and 3-AMPY (TFE:DMF) (d-f) 2D/3D heterostructures thin-films.

To understand the divergent compositional and temporal evolution of the 2D/3D film formation with different ligand solvents, we studied the film structure of the 2D/3D films immediately after spin-coating without further post-treatment (hence dubbed as-spun). To probe the 2D-DJP composition along the cross-section of the film, we employed angle-dependent *ex-situ* GIWAXS at grazing-incidence angles between 0.05 to 0.50° , at a critical angle of 0.15° (Figure 3a, b). The penetration depth as a function of the grazing-incidence angle is calculated and shown in Figure S14. We also performed confocal photoluminescence mapping (CPLM) to selectively observe the photoemission of all 2D-DJPs present in the film (Figures 3b, e) and correlated the observations with SEM (Figures 3c, f).

1 Figure 3a reveals that the overall intensity of $n = 2$ was found to exceed that of
2 $n = 3$ irrespective of the grazing-angle, indicating a film dominated by $n = 2$. However,
3 the integrated area of $n = 2$ sharply increases at lower grazing-incidence angles (i.e.,
4 shallower penetration depth) compared to $n = 3$ and 3D-MHP peak intensity before
5 reaching a maximum at an angle of 0.12° (5 nm x-ray penetration) and becoming
6 invariant thereafter. In contrast, $n = 3$ increased gradually before reaching a maximum
7 at 0.15° (~14 nm). As noted in Figure S14, the x-ray penetration depth sharply
8 increases between 0.12 to 0.15° (by ~10 nm). We infer that the 2D-DJP formation
9 occurs predominantly due to an initial rapid surface physisorption of ligands onto the
10 PbI₂-termination on the reconstructed 3D-MHP interface, forming a strata of $n = 2$,
11 followed by ligand diffusion deeper into the film via the grain boundaries to form a
12 substratum of $n = 3$, forming a graded 2D-MHP capping layer.^[45] CPLM (Figure 3b)
13 revealed that the majority of the emission of the 2D-DJPs in the 3-AMPY (IPA:DMF)
14 sample arises from the central portion of grains and less from the boundaries, with the
15 2D-DJPs getting distributed as platelets on the 3D-MHP surface.
16

17 In contrast, Figure 3d shows that the as-spun 3-AMPY (TFE:DMF) samples
18 display a very different film structure, with the peak intensities of $n = 2, 3$ and 4 phases
19 reaching the maxima at the same angle at 0.15° (~14 nm) and becoming invariant
20 thereafter. We infer that the $n = 2-4$ 2D-DJPs are permuted across the top film surface
21 in mixed domains that extend downwards. The CPLM results (Figure 3e) support this,
22 displaying a more uniform emission throughout the film surface, with comparable PL
23 intensity between the grain boundaries and the perovskite grains. A similar effect was
24 previously reported for ethanol as solvent.^[46] The SEM image (Figure 3f) shows
25 merged and indistinct grain boundaries between 3D-MHPs as a result of 2D-MHPs
26 penetrating deeper into the film microstructure. Thus, TFE:DMF solvent allows a more
27 uniform ligand distribution across the film surface and deeper penetration into grain
28 boundaries, fortifying the 3D-MHP surface. In addition, we found that IPA:DMF and
29 TFE:DMF produce 2D-capping layers of comparable thicknesses for the same ligand
30 concentrations (Figures S14b and c), as both heterostructures reach maximum
31 intensity at the same grazing-incidence.
32
33
34
35
36
37
38
39
40
41
42
43
44
45
46
47
48
49
50
51
52
53
54
55
56
57
58
59
60
61
62
63
64
65

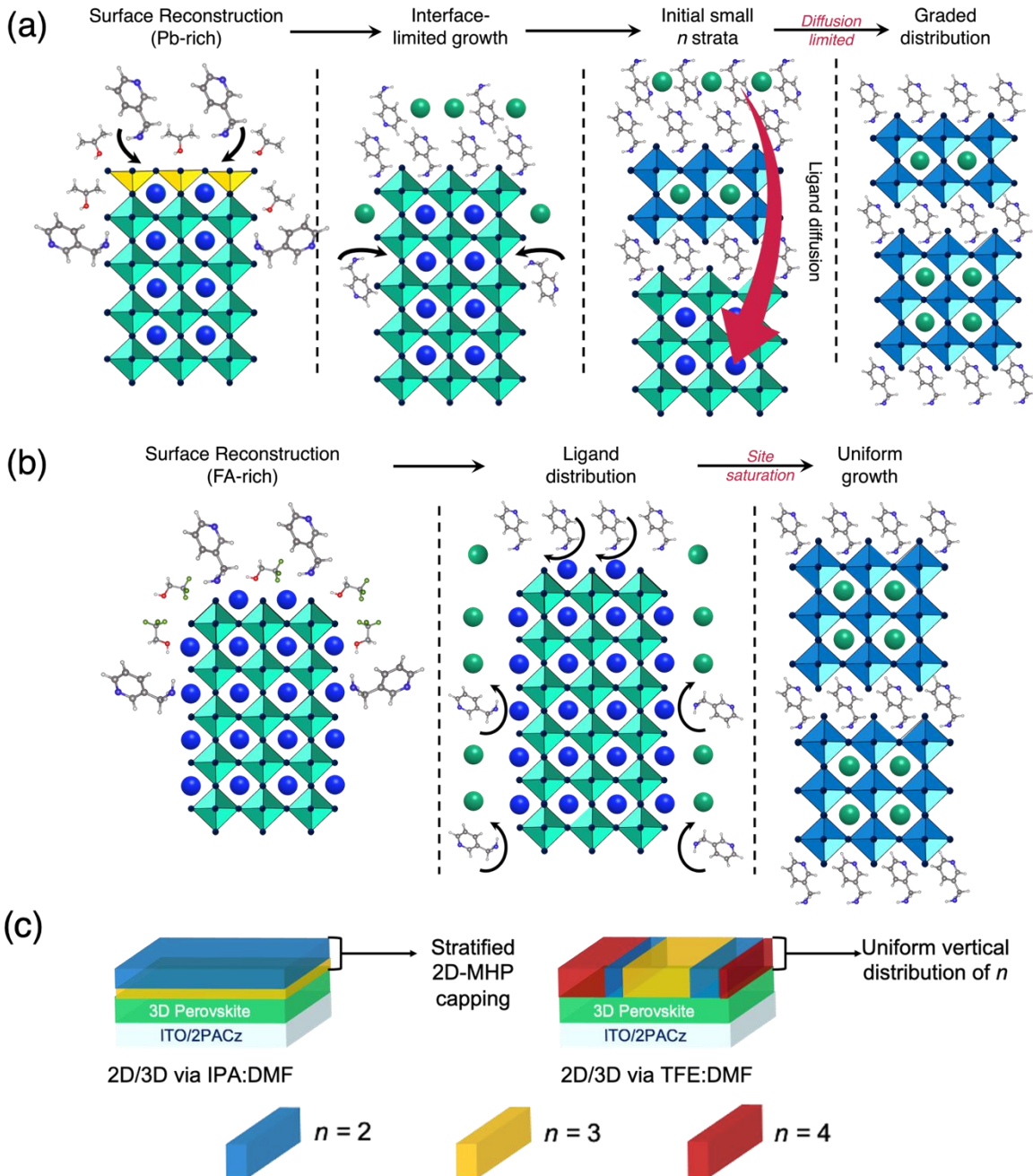


Figure 4. Proposed mechanism depicting surface reconstruction, ligand distribution and 2D-MHP growth in case of (a) 3-AMPY (IPA:DMF) and (b) 3-AMPY (TFE:DMF). (c) Schematic depicting the film structure of as-spun 2D/3D heterostructures fabricated using ligand solutions based on IPA:DMF and TFE:DMF.

Taken collectively, we propose the following formation mechanisms of 2D-DJP on 3D-MHP with IPA:DMF and TFE:DMF solvents in **Figure 4a** and **b**, respectively. The formation of 2D-MHPs with IPA:DMF is precluded by an intermediate state induced by cation leaching by destructive solvents, leading to a reconstructed δ -FAPbI₃/PbI₂-rich surface. The δ -FAPbI₃ and PbI₂ serve as nucleation sites for rapid

1 ligand anchoring via physisorption and subsequent 2D-MHP crystallisation, as ligand-
2 terminated perovskite surfaces are thermodynamically favoured compared to small-
3 cation-termination (Figure 4a).^[47] Eventually, a finite strata of small n (in case of 3-
4 AMPY, $n = 2$) is formed on the reconstructed surface via interface-limited
5 crystallisation. In sequence, a slower diffusion-limited secondary growth occurs at the
6 lower 2D-MHP/3D-MHP interface, leading to the crystallisation of $n \geq 3$. We speculate
7 the ligand-terminated dense small n impede cation diffusion (3-AMPY, MAI) by self-
8 assembly of another layer of unreacted ligands, causing a noticeable time delay in the
9 formation of a sparse larger n strata. The initial surface anchoring and fast reaction of
10 ligands to form small n renders the formation of larger n difficult due to the
11 overconsumption of ligands.
12
13

14 On the other hand, solvent combinations with TFE:DMF do not reconstruct the
15 3D-MHP surface into a PbI_2 -rich state with negligible changes in surface composition
16 ([Figure S5 and S9b](#)). Consequently, very few nucleation sites are available for the
17 bulky ligands to bind on to, favouring uniform ligand distribution at the 3D-MHP surface
18 and grain boundaries with limited physisorption. A downward 2D-DJP formation
19 occurs at roughly the same time scale with different n until the ligands are completely
20 consumed via cation exchange, leading to domains of different n along the cross-
21 section of the 2D-MHP capping layer. Additionally, the inert nature of the TFE:DMF
22 treatment coupled with the relatively low concentration of ligands produced a relatively
23 larger density of $n = 3$ and 4 with minimal damage to the 3D-MHP.
24
25

26 To explore the proposed mechanism in a broader context, we also investigated
27 the formation dynamics of 4-AMPY, a structural isomer of 3-AMPY, for DJP and the
28 more common PEA ligand for RPP ([Figures S15a-b and S16a-b, Supplementary Note](#)
29 [5](#)). The emergent formation dynamics in [Figures S15a-b and S16a-b](#) confirm that the
30 solvent interaction with the 3D-MHP plays a more crucial role in regulating the surface
31 reconstruction and nucleation sites on the 3D-MHP, dictating the sequence of
32 formation of n and relative density of different n -valued 2D-MHPs ([Figure 4a and b,](#)
33 [Figure S15 and 17](#)).
34
35
36
37
38
39
40
41
42
43
44
45
46
47
48
49
50
51
52
53
54
55
56
57
58
59
60
61
62
63
64
65

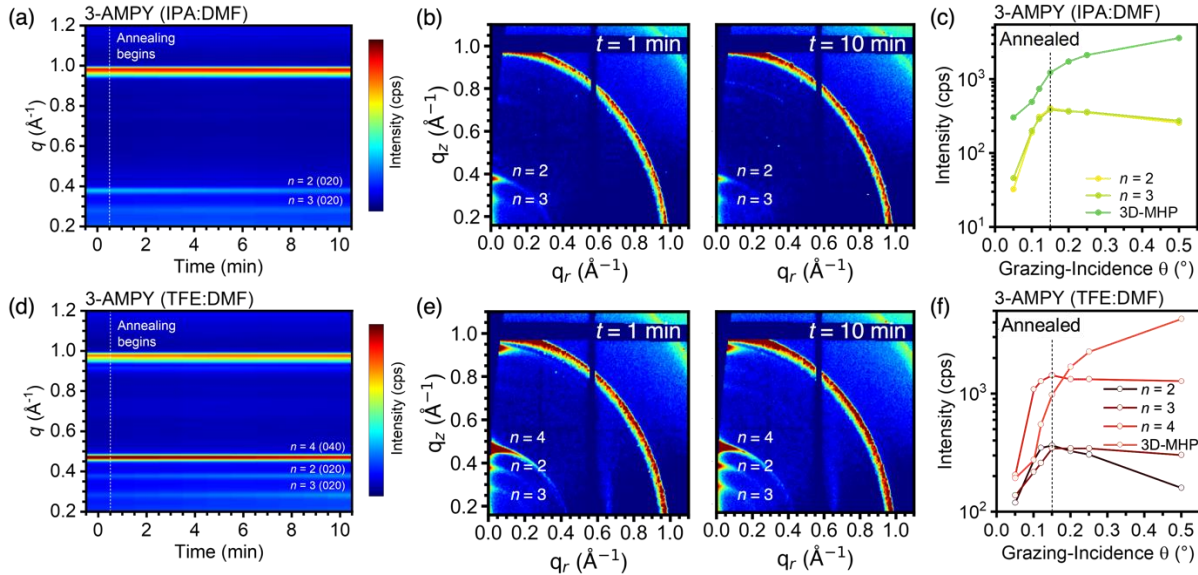


Figure 5. (a), (d) Azimuthally-integrated *in-situ* GIWAXS heat map during thermal annealing with the critical angle (0.15°) marked as a dashed line, (b), (e) individual GIWAXS heat maps at representative timestamps and (c), (f) GIWAXS scattering intensity of 2D-MHPs and 3D-MHP extracted via area-integrated peaks of dominant n as a function of grazing-incidence angle of annealed 3-AMPY (IPA:DMF) (a-c) and 3-AMPY (TFE:DMF) (d-f).

If unreacted ligand diffusion poses a barrier to the formation of 2D/3D heterostructures, annealing should elicit changes in film structure and composition compared to Figures 3a and d.^[48,49] To clearly identify the existence of a possible diffusion-limited formation mechanism in 2D/3D heterostructures, we subjected the as-spun 3-AMPY-treated films to accelerated annealing at RH = 40-50% and T = 130 °C immediately following spin-coating. **Figure 5** display the heatmaps of azimuthally integrated *in-situ* GIWAXS patterns over an annealing period of 10 min, 2D-GIWAXS patterns at specific timestamps and angle-dependent GIWAXS of dominant n DPs at the end of the annealing experiment.

In Figures 5a and b, annealing the 3-AMPY (IPA:DMF) film enabled a transition from a relatively $n = 2$ rich film into a film with an almost equal density of $n = 2$ and 3 phases. The intensity of $n = 2$ (020) peak gradually decreases over the 10 min period, while the $n = 3$ (020) and $n = 4$ (040) peaks remain unchanged (Figures S18a, c). Annealing affords the activation energy required to not only facilitate cation exchange leading to intermixing between $n = 2$ and 3 phases but also the diffusion of unreacted salts (MAI, 3-AMPY) deeper into the perovskite film (via grain boundaries).^[49] On the other hand, annealing induces structural reorganisation in 2D-MHP phase and distribution (Figure 5c). The intensity of both $n = 2$ and 3 rises in tandem at a similar

1 rate, before becoming invariant at 0.15° (~ 14 nm). Evidently, post-annealing
2 transforms the graded phase distribution (Figure 3a) into a uniform mixture of $n = 2$
3 and 3 phases scattered across the 2D-DJP capping layer.
4

5 In Figures 5d and e, annealing the TFE:DMF-treated samples results in minimal
6 change in intensity to $n = 4$ phase, but a gradual increase to $n = 3$ and 2 phases. There
7 is no degradation of the so-formed 2D-MHPs into new lower n polymorphs (Figures
8 5d, S16b and d), whereas **Figure 5f shows that the integrated areas of as-annealed 3-**
9 **AMPY (TFE:DMF) samples exhibit a similar film structure to the as-spun sample with**
10 **the phases becoming invariant at 0.15° (~ 14 nm).** We infer that the $n = 2-4$ 2D-DJPs
11 are uniformly permuted across the height of the film surface in mixed domains with n
12 = 2-4. These trends imply more effective mixing and utilisation of ligands to form 2D-
13 MHPs as early as the spin-coating stage. Thus, the 3-AMPY (TFE:DMF) films are
14 dominated by $n = 3$ and 4 that extend downward onto the 3D-MHP interface (Figure
15 4c, right panel). The energy landscape and reduced compositional drift at elevated
16 temperatures with 2D-MHP capping layer concentrated at $n = 3$ and 4 should be more
17 favourably disposed towards sustained electron tunnelling under extrinsic stressors.
18

29 **2.4. Influence on Photophysics and Recombination Dynamics**

30 Rational solvent selection has thus allowed regulation of 3D-MHP surface
31 termination and nucleation sites to guide the 2D-MHP distribution atop a 3D-MHP
32 template. To close the loop between surface-termination, formation dynamics and
33 translatability to superior solar cell figures of merit, we investigated the implication of
34 solvents and 3D-MHP leaching on the charge transport in PEA, 4-AMPY and 3-AMPY
35 treated films. The extent of solvent-induced leaching of 3D-MHP during the 2D/3D
36 formation is expected to have a noticeable impact on the carrier dynamics of arising
37 films. Static photoluminescence (PL) of representative films on a glass substrate
38 reveals a profound difference between films processed using IPA and TFE.
39 Irrespective of solvent, all 2D/3D films show an appreciable increase in PL signal
40 compared to the pristine 3D-MHP counterpart, with reduced non-radiative
41 recombination (**Figure 6a-c**). However, only TFE:DMF films fully leverage the defect
42 passivation effect of 2D-MHPs by avoiding leaching of the FA^+ / MA^+ during the 2D-
43 treatment to form surfaces with lower non-radiative recombination, bringing forth
44 enhanced PL emission.^[37] In addition, DJP ligands also engender a larger degree of
45 PL enhancement compared to the RPP counterpart due to superior charge transport
46

1 and reduced quantum-confinement (Figures 6b and c).^[50] 4-AMPY treatment brought
2 about a three-fold PL signal enhancement, while 3-AMPY increases five-fold, implying
3 dramatic suppression of non-radiative recombination.^[51] A similar trend is apparent in
4 the time-resolved photoluminescence spectra (TRPL), where longer average lifetimes
5 were recorded for DJP heterojunctions based on TFE:DMF ligand solutions (Figures
6 6d and e, **Figures S19a, c**). We analysed the decay kinetics of the films as a
7 superposition of fast (τ_1) and slow (τ_2) recombination dynamics (Table S2). The fast
8 recombination dynamics are associated with trap-assisted surface recombination,
9 while the slower dynamics are attributed to radiative recombination within the bulk
10 perovskite.^[24,51] In agreement with the PL enhancements in Figures 6a-c, the
11 TFE:DMF treated films unanimously display a prolonged surface recombination
12 lifetimes τ_1 in comparison to their IPA:DMF counterparts, indicating that the latter
13 possesses a certain degree of non-radiative recombination at the 2D-capping
14 interface, possibly due to defect formation and larger density of $n = 2$ phases.^[52] Most
15 uniquely, 3-AMPY-based films demonstrate a monoexponential decay compared to 4-
16 AMPY and PEAI (**Figure S19 a and c**, respectively, Table S2), with a long average
17 lifetime τ_{ave} of 1374 and 1738 ns with IPA:DMF and TFE:DMF, respectively, indicating
18 a significant reduction in surface trap states and efficient passivation.
19
20
21
22
23
24
25
26
27
28
29
30
31
32
33
34
35
36
37
38
39
40
41
42
43
44
45
46
47
48
49
50
51
52
53
54
55
56
57
58
59
60
61
62
63
64
65

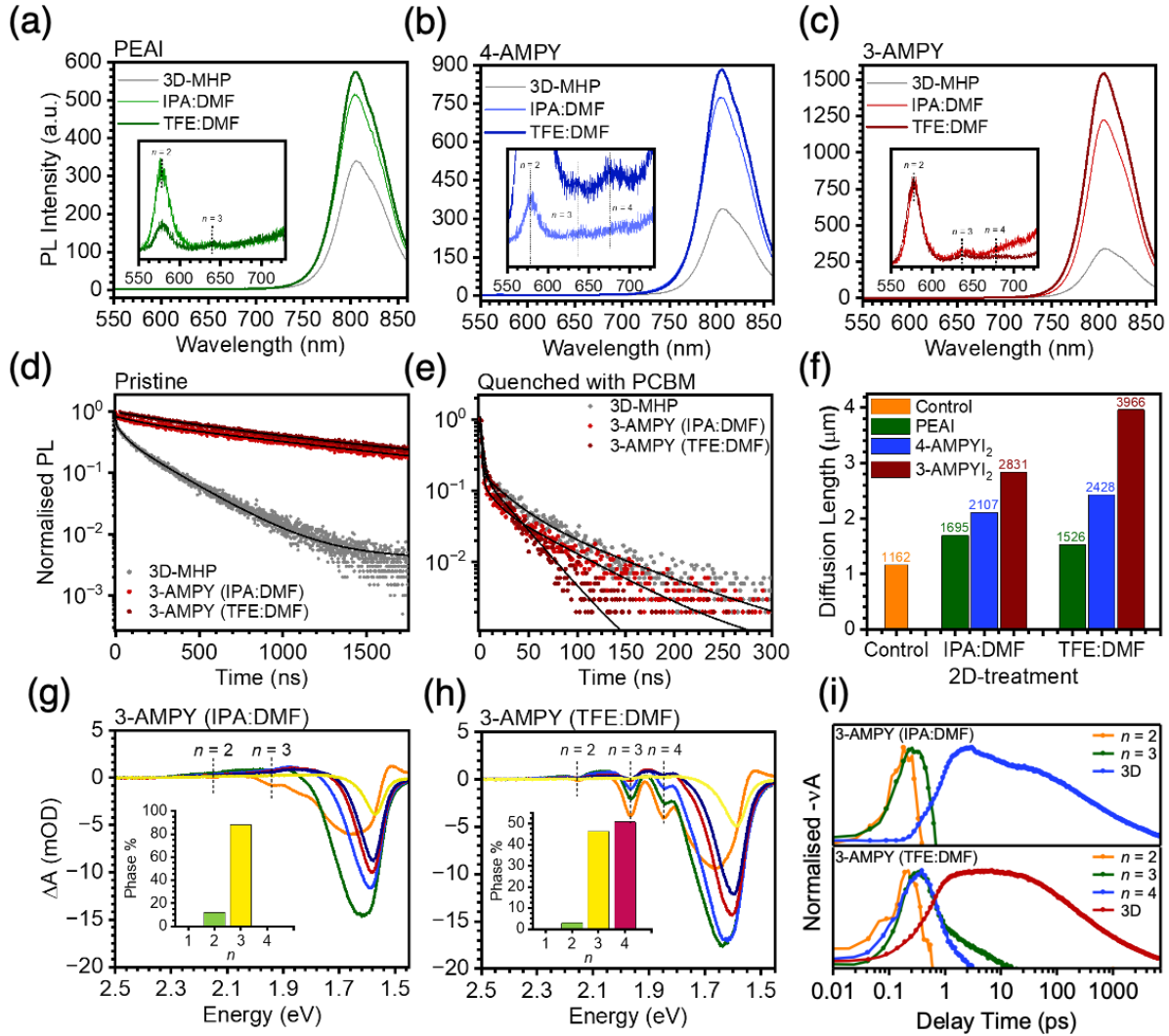


Figure 6. Static PL spectra of 2D/3D heterostructure films comparing 3D-MHP, IPA:DMF- and TFE:DMF-treated films with (a) PEAI, (b) 4-AMPY and (c) 3-AMPY in the ligand solution. TRPL spectra comparing carrier lifetime of (d) bare 3D-MHP, 3-AMPY (IPA:DMF) and 3-AMPY (TFE:DMF) films, respectively, and (e) the same films, with PCBM deposited as an electron quenching layer. (f) Comparison between electron diffusion length based on the extent of PL quenching after deposition of PCBM. Transient Absorption Spectra of 2D/3D heterostructures based on (g) 3-AMPY (IPA:DMF) and (h) 3-AMPY (TFE:DMF). The inset represents the relative quantity of 2D-DJPs present on the film based on the maximum amplitude of bleach peak indicating 2D-DJP presence. (i) Comparison between charge cascading kinetics of 3-AMPY (IPA:DMF) and 3-AMPY (TFE:DMF) films.

To verify the translatability of these insights to p-i-n PSCs, we studied the degree of PL quenching and electron diffusion length when an ETL (PC_{61}BM) is deposited atop the films. The 2D/3D films have a strong degree of PL quenching compared to the pristine 3D-MHP films (Figures 6e, S19b and d). The diffusion length

1 for electrons can be evaluated by comparing the slow recombination dynamics τ_2 of
2 the quenched and pristine films. The quenched carrier lifetimes and diffusion length
3 values are summarised in Table S3. The approximate value of diffusion length L_D was
4 estimated using the following equation suggested by Snaith et al^[53]:

5

6

7
$$L_D = \frac{2d}{\pi} \sqrt{2 \left(\frac{\tau_2}{\tau_{2,quenched}} - 1 \right)}, \quad (2)$$

8

9

10 The pristine 3D-MHP has an electron diffusion length of 1162 nm, which is
11 typical for a triple-cation perovskite film. In comparison, 2D/3D heterostructures exhibit
12 an elongated electron diffusion length (Figure 6f). The 3-AMPY (IPA:DMF) and 3-
13 AMPY (TFE:DMF) films demonstrate nearly three-fold and four-fold enhancement of
14 electron diffusion lengths at 2831 and 3996 nm, respectively. Overall, these
15 measurements validate that due to the stratified nature of 2D/3D films via IPA:DMF
16 treatment and the presence of $n = 2$ phases, the electron diffusion length is lower than
17 that of the TFE:DMF sample which contains a uniform vertical n distribution with larger
18 density of $n > 2$ phases.

19 As the surface phase composition has a profound impact on the charge transfer
20 between 2D and 3D-MHPs, we performed femtosecond transient absorption
21 spectroscopy (TAS) on the 3D-MHP and 2D/3D films to accurately identify the phase
22 distribution of different 2D capping layers.^[24,26] Figures 6g-h denote the TAS linecuts
23 of representative 3-AMPY-based 2D/3D heterostructures taken at specific delay times
24 to reflect the time taken by the charge carriers to fully populate the ground states of
25 different n -value phases and display the maximum photobleaching before funnelling
26 to the 3D-MHPs. 3-AMPY (IPA:DMF) samples present three bleach peaks
27 corresponding to $n = 2$ (2.14 eV), $n = 3$ (1.94 eV) and 3D-MHP at 1.56 eV, consistent
28 with the band-edges of the respective species.^[31] A relatively low intensity bleach peak
29 of $n = 2$ and dominant $n = 3$ peak indicates that the $n = 3$ (3-AMPY)MA₂Pb₃I₁₀ phase
30 is formed in the majority. The 3-AMPY (TFE:DMF) samples exhibit bleach peaks
31 corresponding to $n = 2, 3, 4$ and 3D-MHP, with relatively larger bleaching by $n = 3$ and
32 4. Using the maximum amplitudes of the ground state bleaching peaks (GSBs), the
33 percentage contribution of each 2D-DJP phase can be estimated as shown in the inset
34 of Figures 6g and h. 3-AMPY (TFE:DMF) treatment has afforded the formation of $n =$
35 3 and 4 in the majority, contributing to almost 90% of total 2D-DJP content. These
36 results also confirm the formation of films dominated by $n = 3$ and 4 during *in-situ* and
37 *ex-situ* GIWAXS of TFE:DMF samples and further explain the trends observed in the
38

PL study. While IPA:DMF does indeed considerably extend the electron diffusion length due to defect passivation, the large density of $n = 2$ phase present can pose an impediment to charge tunnelling due to the large quantum-confinement of small- n . In contrast, the TFE:DMF treatment appears to generate DJP_s concentrated around $n = 3$ and 4, which should serve as a suitable sweet spot for balancing the enhanced stability of 2D-DJP_s while sufficiently low electron tunnelling barrier. We observed similar phase distribution dominated by $n = 3$ and 4 in the TAS kinetics of 4-AMPY (TFE:DMF) as noted in [Figure S20](#), confirming that TFE is a promising post-processing solvent towards fabricating efficient solar cells capable of generating fewer defects.

Charge carrier dynamics were then elucidated to exemplify the charge build-up and decay (Figure 6i). In 3-AMPY (IPA:DMF), the charge accumulation occurs within 0.1 ps for $n = 2$ and 3, followed by photobleaching decay at 0.3 and 1 ps, respectively. The rapid decay of the 2D-DJP_s indicates rapid charge transfer between 2D-DJP_s. Subsequently, the 1.56 eV peak of 3D-MHP gradually builds up reaching a maximum at 2 ps before decaying over 7 ns. While the rapid bleaching of the $n = 2$ phase suggests that there is no apparent charge accumulation in the $n = 2$ phase, the delay in the build-up of the 3D-MHP implies a slower 2D-to-3D charge transfer. Like 3-AMPY (IPA:DMF), 3-AMPY (TFE:DMF) sample exhibit a rapid build-up of charge carriers occurring within 0.1 ps for $n = 2$ and 0.2 ps for $n = 3$ and 4 followed by decay over 1, and 10 ps, respectively. The rise of the 3D-MHP occurs at 0.1 ps, eventually reaching a maximum in less than 2 ps before decaying over 7 ns.

The decay kinetics are extracted by curve fitting the amplitude of the 3D-MHP GSB to multi-exponential functions as listed below:

$$\Delta A = a_1 e^{\frac{-t}{\tau_1}} + a_2 e^{\frac{-t}{\tau_2}} + a_3 e^{\frac{-t}{\tau_3}} - c_1 e^{\frac{-t}{\tau_{et}}}, \quad (3)$$

where the amplitude is expressed as a convolution of a first-order decay lifetime (τ_1) and energy transfer across phases (τ_{et}) and two slow decay components, ascribed to bimolecular (τ_2) and excitonic trap recombination (τ_3).^[54] We have discussed the trends of the fast decay components in this work. We found the energy transfer time constant τ_{et} to be 5.08 and 0.48 ps for 3-AMPY (IPA:DMF) and 3-AMPY (TFE:DMF), respectively. The shorter τ_{et} and rapid rise of the 3D peak can be attributed to the efficient interphase transfer process; the presence of larger n fragments with reduced quantum confinement may lead to efficient charge dissociation at the 2D/3D interface. Furthermore, the bleaching peak of the 3D-components reveals a first-order decay

1 time of 138 and 146 ps, respectively, also suggesting a lower density of traps in line
2 with the PL results.

3 **2.5. Energy landscape and photovoltaic efficiency**

4 Modulating the n distribution across the 2D/3D heterostructure, the defects
5 formed during solvent-induced surface reconstruction and cation choice should
6 collectively influence the energy landscape of the 2D/3D heterostructure towards
7 reducing electron blocking at the film/ETL interface. To examine these effects, we
8 performed surface-sensitive UPS on the 2D/3D films to measure the VBM and fermi-
9 level (E_f) from the top few nm of the films. We performed the energy level calculations
10 based on the fermi level of silver reference ([Figure S21a](#)), optical bandgap ([Figure](#)
11 [S21b](#)) and cut-offs extracted from [Figures S22a-f](#) and summarised in Table S4. UPS
12 spectra of the 3D-MHP revealed a typical band structure for a triple-cation 3D-MHP
13 with a VBM at -5.60 eV and E_f of -4.72 eV, implying a slightly more n-type behaviour
14 which is typical for Pb-based perovskites ([Figure 7a](#)). 2D/3D heterostructures with
15 PEAI as cation led to significant downshifting of the VBM and E_f to -5.86 eV and -4.91
16 eV, respectively, attributed to the stronger quantum confinement effect prevalent in
17 2D-RPPs ([Figure S23a](#)). Similar passivation methods have a comparable downshift in
18 VBM when PEAI was used as a passivator (c.a. 0.2 eV).^[17,18] This trend is also
19 consistent with the observed UPS spectra of the $n = 3$ 2D-MHP films in Figure 1c. On
20 the other hand, 3-AMPY (Figure 6a) and 4-AMPY ([Figure S23a](#)) ligands result in
21 shallower VBM because of the shorter interlayer spacing between adjacent inorganic
22 frameworks affording stronger I-I antibonding interactions.^[34] 3-AMPY benefitted from
23 the smallest interlayer spacing of 3.6 Å and possessed the smallest VBM offsets of
24 c.a. 0.06-0.09 eV with respect to the 3D-MHP.

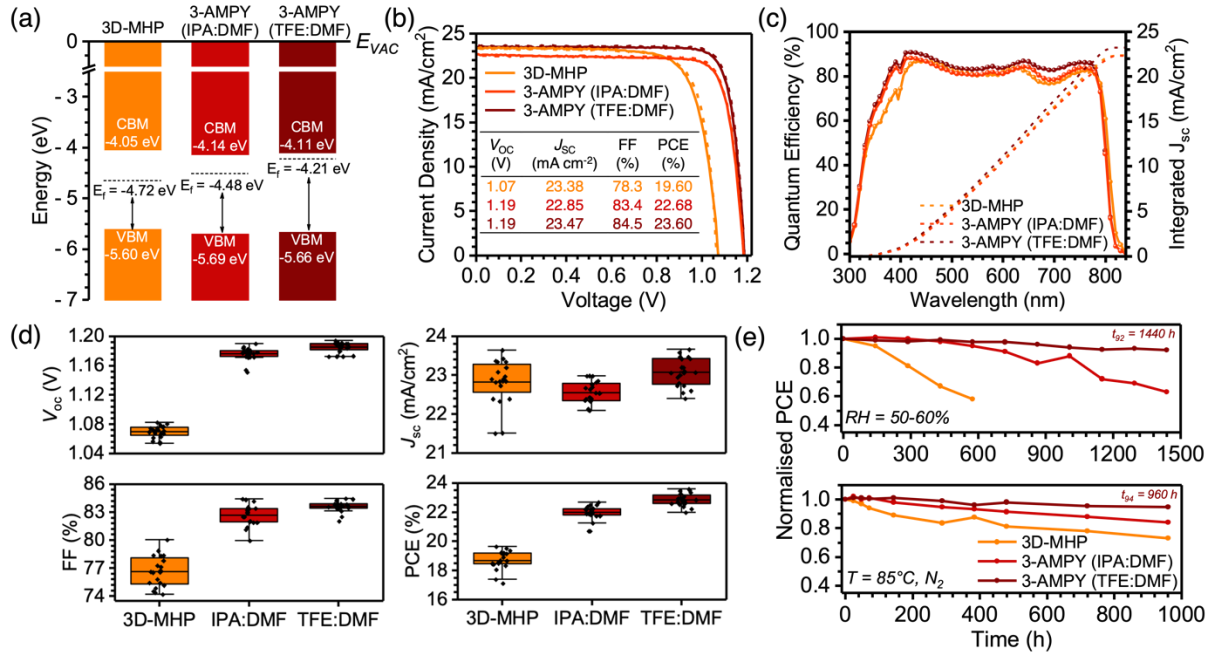


Figure 7. (a) Energy level diagram of pristine 3D-MHP and 3-AMPY DJP heterostructures. **(b)** Device performance of PSCs containing pristine 3D-MHP and 3-AMPY (IPA:DMF) and 3-AMPY (TFE:DMF) heterostructures: **(c)** forward (solid) and reverse (dotted) current density-voltage curves (J-V), **(d)** external quantum efficiency (EQE) and integrated short-circuit current density, **(d)** statistics of photovoltaic characteristics of reverse scans of PSCs, and **(e)** stability of best-performing PSCs under ambient conditions (RH = 50-60%) (top) and under persistent thermal stress at 85°C (bottom).

Interestingly, we found very little difference in VBM position upon varying solvent for a selected ligand (Figures 7a and S23b). However, there is a profound influence on the E_f and CBM location with increasing n . We observed strikingly shallower E_f s for DJP-based 2D/3D heterostructures fabricated via TFE:DMF solvent compared to their 3D-MHP counterparts irrespective of ligand (Figure S23a). The E_f of 2D-MHPs also tends to shift towards increasingly n-type behaviour with decreasing quantum-confinement. IPA:DMF treated films possess large trap density, as evidenced by TRPL even after passivation. Leaching of small cations from the perovskite surface causes local FA^+/MA^+ deficiencies resulting in a more p-type nature (IPA:DMF), while one rich in organic cations exhibits n-type behaviour (e.g., TFE:DMF). Most notably, 3-AMPY (TFE:DMF) leverages the formation of large n and low defect density to yield a E_f of -4.21 eV, creating favourable band bending with the CBM of the 3D-MHP for electron extraction (Figure 7a).

Motivated by the favourable energy landscape and charge carrier dynamics, we examined the impact of the new solvent treatment of forming 2D/3D heterostructures on the solar cell characteristics of a typical p-i-n stack: ITO | 2PACz | Perovskite | PCBM | C₆₀ | BCP | Ag with different surface treatments (PEAI, 4-AMPY, and 3-AMPY in IPA:DMF or TFE:DMF, **Figure S24**). In agreement with our findings that reducing the quantum confinement via rational ligand selection leads to more efficient carrier extraction and electron tunnelling, 3-AMPY-based 2D/3D heterostructures unanimously outperform the 4-AMPY and PEAI-treated devices. The elimination of the Van der Waals gap in the DJP capping layers has afforded improvements in FF compared to the RPP capping layer from PEAI, while the fine-tuned band alignment of 3-AMPY devices results in a reduced electron tunnelling barrier with dramatic improvements in V_{oc} up to 1.19 V (Figure 7b). Moreover, in agreement with our findings that TFE:DMF treatment results in a uniformly mixed 2D-DJP capping layer dominated by $n \geq 3$ phases that enables long electron diffusion lengths, the 3-AMPY (TFE:DMF) devices have outperformed the 3-AMPY (IPA:DMF), as shown in Figure 7b. The improved performance of the TFE:DMF solar cells compared to the IPA:DMF counterparts arises from a slight increase in FF and J_{sc} (83.4 to 84.5% and 22.85 to 23.47 mA/cm² for 3-AMPY, respectively). As a result, a champion device efficiency of 23.60% was obtained. The J_{sc} of 23.47 mA/cm² is also within a 5% mismatch of the integrated current density from the EQE spectra (23.1 mA/cm²) in Figure 7c. Further analysing the EQE spectrum of the champion device via the first derivative reveals a bandgap of 1.55 eV, recording a voltage loss (V_{oc}^{loss}) of 0.36 V (**Figure S25**). The improvements in these solar cell figure of merits validate the translatability of the observed enhancements in carrier dynamics, elongated electron diffusion and interfacial band alignment which stem from tailoring 2D-DJP phase distribution atop the 3D-MHP via an inert 2D-DJP processing solvent. **The combined enhancement of the photovoltaic characteristics was verified statistically through a comparison of 20 individual devices, with an average PCE of 18.71% \pm 0.65% for the 3D-MHP, 21.92 % \pm 0.53% for the 3-AMPY (IPA:DMF) and 22.98% \pm 0.35% for the 3-AMPY (TFE:DMF), respectively (Figure 7d).**

Finally, we investigated the long-term stability of the devices to verify the resilience of the 2D/3D heterostructures towards ambient and thermal stress. In practice, 2D/3D perovskites have been shown to display a drop in PCE under persistent thermal stress over a few hours.^[55] Thus, it is critical to ascertain the

1 ambient and thermal stability (Supplementary Note 6, Figure S26) of the new ligands
2 used in our study. We subjected solar cells of 3-AMPY and PEAI heterostructures from
3 the representative solvents used in this study and periodically monitored their PCEs
4 under the influence of relative humidity (RH = 50-60%, Figure 7e top panel, Figure
5 S26) and temperature (85°C, Figure 7e bottom panel, Figure S27). The 3D-MHP
6 PSCs drop to 58% of their original PCE within 600 h of ambient exposure. However,
7 2D treatment has significantly prolonged the shelf-life of the PSCs. In particular, the
8 devices fabricated via TFE:DMF solvent have retained 90% and 92% of their original
9 PCEs after 1500 h with PEAI and 3-AMPY as the respective ligands. In stark contrast,
10 the IPA:DMF based films degrade rapidly to c.a. 65% after a similar timeframe,
11 confirming our hypothesis that exposing the $[PbI_6]^{4-}$ framework of the 3D-MHP during
12 post-treatment using surface destructive solvent (IPA:DMF) is a suboptimal
13 passivation method that generates surface defects.

14 More critically, the 2D-treated films also exhibit curious trends during thermal
15 stress tests. Particularly, the PEAI-based 2D/3D devices are characterised by an initial
16 rapid fall in PCE to c.a. 73% of their original values, followed by a period of relative
17 stability up to 384 h. The PEAI (TFE:DMF) devices eventually drop to 47% of their
18 original PCEs in 1000 h, with overall lower device stability compared to the 3D-MHP
19 counterparts (Figure S28). 3-AMPY (TFE:DMF) on the other hand exhibits a t_{92} of 960
20 h, while 3-AMPY (IPA:DMF) retains 83% of its original PCE, proving that mitigating
21 surface reconstruction is a more efficient route to fabricating 2D/3D heterostructures.
22 Thus, we are able to leverage the rigid lattice and superior charge transport of 2D-
23 DJP_s as capping layers without sacrificing the structural integrity of the underlying 3D-
24 MHP_s to fabricate efficient and stable solar cells.

44 3. Conclusion.

45 In summary, we compared the solvent-mediated formation dynamics of 2D-on-3D
46 perovskites and translated the insights to tailor the energy landscape, enabling
47 efficient and stable inverted perovskite solar cells via synergistic ligand engineering.
48 Fabricating 2D/3D heterostructures with IPA as a processing solvent leads to
49 diffusion-limited formation of a graded 2D-capping layer with smaller n initially at the
50 top 2D-MHP surface, and larger n later, buried closer to the 2D/3D heterostructure
51 interface. In contrast, TFE allows crystallisation of larger n first and smaller n very
52 shortly after, forming uniformly distributed domains along the cross section of the 2D-
53 MHP_s.
54

1 MHP layer. Additionally, using DJP-forming ligands 3-AMPY and 4-AMPY in
2 conjunction with TFE enabled formation of 2D-capping layers dominated by $n = 3$ and
3 4. The preponderance of large n DJPs in the capping layer significantly reduced defect
4 density, elongated electron diffusion length and created favourable band bending to
5 facilitate efficient electron tunnelling. As a result, inverted 2D/3D PSCs based on 3-
6 AMPY and TFE-based solvent leverage these advantages to deliver a champion
7 power conversion efficiency of 23.60% with a remarkable V_{oc} and FF of 1.19 V and
8 84.5%, respectively, with high stability towards moisture ingress and thermal stress.
9 Taken together, the interplay between surface states before passivation, emergent
10 formation dynamics of 2D/3D heterostructures and band energy modulation with DJPs
11 will further guide the experimental and theoretical design of efficient and stable p-i-n
12 solar cells through surface engineering.
13
14
15
16
17
18
19
20
21
22
23
24
25
26
27
28
29
30
31
32
33
34
35
36
37
38
39
40
41
42
43
44
45
46
47
48
49
50
51
52
53
54
55
56
57
58
59
60
61
62
63
64
65

1
2
3
4
5
6
7
4. Supporting Information

8
9
10 Supporting Information is available from the Wiley Online Library or from the
11 author.
12
13
14
15
16
17
18
19
20
21
22

23
24
5. Acknowledgements

25
26
27
28
29
30
31
32
33
34
35
36
37
38
39
40
41
42
43
44
45
46
47
48
49
50
51
52
53
54
55
56
57
58
59
60
61
62
63
64
65
This work was financially supported by NSF ECCS-2054942 and EPM-2114350. This work made use of the Cornell Center for Materials Research Shared Facilities which are supported through the NSF MRSEC program (DMR-1719875) and the GIWAXS and TAS from the resources of the Centre for Functional Nanomaterials and the CMS beamline (11-BM) of the National Synchrotron Light Source II, both supported by U.S. DOE Office of Science Facilities at Brookhaven National Laboratory under Contract No. DE-SC0012704.

23
24
6. Conflicting Interest

25
26
The authors declare no competing interests.
27
28
29
30
31
32
33
34
35
36
37
38
39
40
41
42
43
44
45
46
47
48
49
50
51
52
53
54
55
56
57
58
59
60
61
62
63
64
65

23
24
7. Data Availability Statement

25
26
The data that support the findings of this study are available from the corresponding
27 author upon reasonable request.
28
29
30
31
32
33
34
35
36
37
38
39
40
41
42
43
44
45
46
47
48
49
50
51
52
53
54
55
56
57
58
59
60
61
62
63
64
65

8. References

[1] X. Li, J. M. Hoffman, M. G. Kanatzidis, *Chem Rev* **2021**, *121*, 2230.

[2] P. Liu, N. Han, W. Wang, R. Ran, W. Zhou, Z. Shao, *Advanced Materials* **2021**, *33*, 2002582.

[3] B. Saparov, D. B. Mitzi, *Chem Rev* **2016**, *116*, 4558.

[4] Y. Gao, E. Shi, S. Deng, S. B. Shiring, J. M. Snaider, C. Liang, B. Yuan, R. Song, S. M. Janke, A. Liebman-Peláez, P. Yoo, M. Zeller, B. W. Boudouris, P. Liao, C. Zhu, V. Blum, Y. Yu, B. M. Savoie, L. Huang, L. Dou, *Nat Chem* **2019**, *11*, 1151.

[5] L. Mao, C. C. Stoumpos, M. G. Kanatzidis, *J Am Chem Soc* **2019**, *141*, 1171.

[6] Z. Xu, D. Lu, X. Dong, M. Chen, Q. Fu, Y. Liu, *Advanced Materials* **2021**, *33*, 2105083.

[7] S. Sidhik, Y. Wang, W. Li, H. Zhang, X. Zhong, A. Agrawal, I. Hadar, I. Spanopoulos, A. Mishra, B. Traoré, M. H. K. Samani, C. Katan, A. B. Marciel, J. C. Blancon, J. Even, A. Kahn, M. G. Kanatzidis, A. D. Mohite, *Cell Rep Phys Sci* **2021**, *2*.

[8] M. Shao, T. Bie, L. Yang, Y. Gao, X. Jin, F. He, N. Zheng, Y. Yu, X. Zhang, *Advanced Materials* **2022**, *34*, 2107211.

[9] Z. Li, B. Li, X. Wu, S. A. Sheppard, S. Zhang, D. Gao, N. J. Long, Z. Zhu, *Science* **2022**, *376*, 416.

[10] H. J. Mun, M. G. Kim, T. J. Shin, S. Il Seok, *Nature* **2023**, *616*, 724.

[11] T. Yang, L. Gao, J. Lu, C. Ma, Y. Du, P. Wang, Z. Ding, S. Wang, P. Xu, D. Liu, H. Li, X. Chang, J. Fang, W. Tian, Y. Yang, *Nat Energy* **2023**, *14*, 839.

[12] M. A. Mahmud, T. Duong, J. Peng, Y. Wu, H. Shen, D. Walter, H. T. Nguyen, N. Mozaffari, G. D. Tabi, K. R. Catchpole, K. J. Weber, T. P. White, *Adv Funct Mater* **2022**, *32*, 2009164.

[13] J. W. Lee, S. Tan, S. Il Seok, Y. Yang, N. G. Park, *Science* **2022**, *375*.

[14] A. A. Sutanto, P. Caprioglio, N. Drigo, Y. J. Hofstetter, I. Garcia-Benito, V. I. E. Queloz, D. Neher, M. K. Nazeeruddin, M. Stolterfoht, Y. Vaynzof, G. Grancini, *Chem* **2021**, *7*, 1903.

[15] G. Wu, R. Liang, M. Ge, G. Sun, Y. Zhang, G. Xing, *Advanced Materials* **2022**, *34*, 2105635.

[16] X. Lin, D. Cui, X. Luo, C. Zhang, Q. Han, Y. Wang, L. Han, *Energy Environ Sci* **2020**, *13*, 3823.

[17] S. Gharibzadeh, P. Fassl, I. M. Hossain, P. Rohrbeck, M. Frericks, M. Schmidt, T. Duong, M. R. Khan, T. Abzieher, B. A. Nejand, F. Schackmar, O. Almora, T. Feeney, R. Singh, D. Fuchs, U. Lemmer, J. P. Hofmann, S. A. L. Weber, U. W. Paetzold, *Energy Environ Sci* **2021**, *14*, 5875.

[18] Y. Huang, K. Yan, B. Niu, Z. Chen, E. Gu, H. Liu, B. Yan, J. Yao, H. Zhu, H. Chen, C.-Z. Li, *Energy Environ Sci* **2023**, *16*, 557.

[19] M. G. La-Placa, L. Gil-Escrig, D. Guo, F. Palazon, T. J. Savenije, M. Sessolo, H. J. Bolink, *ACS Energy Lett* **2019**, *4*, 2893.

[20] S. Sidhik, Y. Wang, M. De Siena, R. Asadpour, A. J. Torma, T. Terlier, K. Ho, W. Li, A. B. Puthirath, X. Shuai, A. Agrawal, B. Traore, M. Jones, R. Giridharagopal, P. M. Ajayan, J. Strzalka, D. S. Ginger, C. Katan, M. A. Alam, J. Even, M. G. Kanatzidis, A. D. Mohite, *Science* **2022**, *377*, 1425.

[21] X. Zhong, X. Ni, S. Sidhik, H. Li, A. D. Mohite, J. L. Brédas, A. Kahn, *Adv Energy Mater* **2022**, *12*, 1.

[22] T. Kodalle, R. F. Moral, L. Scalon, R. Szostak, M. Abdelsamie, P. E. Marchezi, A. F. Nogueira, C. M. Sutter-Fella, *Adv Energy Mater* **2022**.

[23] M. He, J. Liang, Z. Zhang, Y. Qiu, Z. Deng, H. Xu, J. Wang, Y. Yang, Z. Chen, C. C. Chen, *J Mater Chem A Mater* **2020**, 8, 25831.

[24] Y. Du, Q. Tian, S. Wang, T. Yang, L. Yin, H. Zhang, W. Cai, Y. Wu, W. Huang, L. Zhang, K. Zhao, S. Liu, *Advanced Materials* **2022**, 35, 2206451.

[25] K. Ma, J. Sun, H. R. Atapattu, B. W. Larson, H. Yang, D. Sun, K. Chen, K. Wang, Y. Lee, Y. Tang, A. Bhoopalam, L. Huang, K. R. Graham, J. Mei, L. Dou, *Sci Adv*, **2023**, 9.

[26] H. Chen, S. Teale, B. Chen, Y. Hou, L. Grater, T. Zhu, K. Bertens, S. M. Park, H. R. Atapattu, Y. Gao, M. Wei, A. K. Johnston, Q. Zhou, K. Xu, D. Yu, C. Han, T. Cui, E. H. Jung, C. Zhou, W. Zhou, A. H. Proppe, S. Hoogland, F. Laquai, T. Filleter, K. R. Graham, Z. Ning, E. H. Sargent, *Nat Photonics* **2022**, 16, 358.

[27] S. Tan, T. Huang, I. Yavuz, R. Wang, M. H. Weber, Y. Zhao, M. Abdelsamie, M. E. Liao, H. C. Wang, K. Huynh, K. H. Wei, J. Xue, F. Babbe, M. S. Goorsky, J. W. Lee, C. M. Sutter-Fella, Y. Yang, *J Am Chem Soc* **2021**, 143, 6781.

[28] S. Tan, I. Yavuz, M. H. Weber, T. Huang, C. H. Chen, R. Wang, H. C. Wang, J. H. Ko, S. Nuryyeva, J. Xue, Y. Zhao, K. H. Wei, J. W. Lee, Y. Yang, *Joule* **2020**, 4, 2426.

[29] X. Xiao, M. Wu, Z. Ni, S. Xu, S. Chen, J. Hu, P. N. Rudd, W. You, J. Huang, *Advanced Materials* **2020**, 32, 2004080.

[30] C. C. Stoumpos, D. H. Cao, D. J. Clark, J. Young, J. M. Rondinelli, J. I. Jang, J. T. Hupp, M. G. Kanatzidis, *Chemistry of Materials* **2016**, 28, 2852.

[31] X. Li, W. Ke, B. Traoré, P. Guo, I. Hadar, M. Kepenekian, J. Even, C. Katan, C. C. Stoumpos, R. D. Schaller, M. G. Kanatzidis, *J Am Chem Soc* **2019**, 141, 12880.

[32] Z. Shi, Z. Ni, J. Huang, *ACS Energy Lett* **2022**, 7, 984.

[33] X. Li, W. Ke, B. Traoré, P. Guo, I. Hadar, M. Kepenekian, J. Even, C. Katan, C. C. Stoumpos, R. D. Schaller, M. G. Kanatzidis, *J Am Chem Soc* **2019**, 141, 12880.

[34] R. Prasanna, A. Gold-Parker, T. Leijtens, B. Conings, A. Babayigit, H. G. Boyen, M. F. Toney, M. D. McGehee, *J Am Chem Soc* **2017**, 139, 11117.

[35] Y. Fu, T. Wu, J. Wang, J. Zhai, M. J. Shearer, Y. Zhao, R. J. Hamers, E. Kan, K. Deng, X. Y. Zhu, S. Jin, *Nano Lett* **2017**, 17, 4405.

[36] R. Azmi, E. Ugur, A. Seitkhan, F. Aljamaan, A. S. Subbiah, J. Liu, G. T. Harrison, M. I. Nugraha, M. K. Eswaran, M. Babics, Y. Chen, F. Xu, T. G. Allen, A. Rehman, C. Wang, T. D. Anthopoulos, U. Schwingenschlögl, M. De Bastiani, E. Aydin, S. De Wolf, *Science* **2022**, 5784, 1.

[37] J. J. Yoo, S. Wieghold, M. C. Sponseller, M. R. Chua, S. N. Bertram, N. T. P. Hartono, J. S. Tresback, E. C. Hansen, J. P. Correa-Baena, V. Bulović, T. Buonassis, S. S. Shin, M. G. Bawendi, *Energy Environ Sci* **2019**, 12, 2192.

[38] A. H. Proppe, A. Johnston, S. Teale, A. Mahata, R. Quintero-Bermudez, E. H. Jung, L. Grater, T. Cui, T. Filleter, C. Y. Kim, S. O. Kelley, F. De Angelis, E. H. Sargent, *Nat Commun* **2021**, 12, 1.

[39] D. Zhang, H. Zhang, H. Guo, F. Ye, S. Liu, Y. Wu, *Adv Funct Mater* **2022**, 32.

[40] J. Hou, W. Li, H. Zhang, S. Sidhik, J.-C. Blancon, J. Even, M. G. Kanatzidis, A. D. Mohite, **2022**.

[41] M. Avrami, *J Chem Phys* **1939**, 7, 1103.

[42] M. Avrami, *J Chem Phys* **1940**, 8, 212.

[43] M. Avrami, *J Chem Phys* **1941**, 9, 177.

[44] J. Dong, S. Shao, S. Kahmann, A. J. Rommens, D. Hermida-Merino, G. H. ten Brink, M. A. Loi, G. Portale, *Adv Funct Mater* **2020**, 30.

[45] Y. Fu, W. Zheng, X. Wang, M. P. Hautzinger, D. Pan, L. Dang, J. C. Wright, A. Pan, S. Jin, *J Am Chem Soc* **2018**, *140*, 15675.

[46] J. Xi, J. Jiang, H. Duim, L. Chen, J. You, G. Portale, S. (Frank) Liu, S. Tao, M. A. Loi, *Advanced Materials* **2023**, *35*, 2302896.

[47] A. Jana, Q. Ba, A. S. Nissimagoudar, K. S. Kim, *J Mater Chem A Mater* **2019**, *7*, 25785.

[48] F. Ji, L. Wang, S. Pang, P. Gao, H. Xu, G. Xie, J. Zhang, G. Cui, *J Mater Chem A Mater* **2016**, *4*, 14437.

[49] C. Zhang, S. Wu, L. Tao, G. M. Arumugam, C. Liu, Z. Wang, S. Zhu, Y. Yang, J. Lin, X. Liu, R. E. I. Schropp, Y. Mai, *Adv Energy Mater* **2020**, *10*, 1.

[50] T. He, S. Li, Y. Jiang, C. Qin, M. Cui, L. Qiao, H. Xu, J. Yang, R. Long, H. Wang, M. Yuan, *Nat Commun* **2020**, *11*, 1.

[51] M. Kaiser, Y. Li, I. Allegro, B. S. Richards, U. W. Paetzold, I. A. Howard, *Adv Mater Interfaces* **2021**, *8*, 2101326.

[52] S. Shao, H. Duim, Q. Wang, B. Xu, J. Dong, S. Adjokatse, G. R. Blake, L. Protesescu, G. Portale, J. Hou, M. Saba, M. A. Loi, *ACS Energy Lett* **2020**, *5*, 39.

[53] M. J. P. Alcocer, T. Leijtens, L. M. Herz, A. Petrozza, H. J. Snaith, *Science (1979)* **2013**, *342*, 341.

[54] J. Liu, J. Leng, K. Wu, J. Zhang, S. Jin, *J Am Chem Soc* **2017**, *139*, 1432.

[55] A. A. Sutanto, R. Szostak, N. Drigo, V. I. E. Queloz, P. E. Marchezi, J. C. Germino, H. C. N. Tolentino, M. K. Nazeeruddin, A. F. Nogueira, G. Grancini, *Nano Lett* **2020**, *20*, 3992.

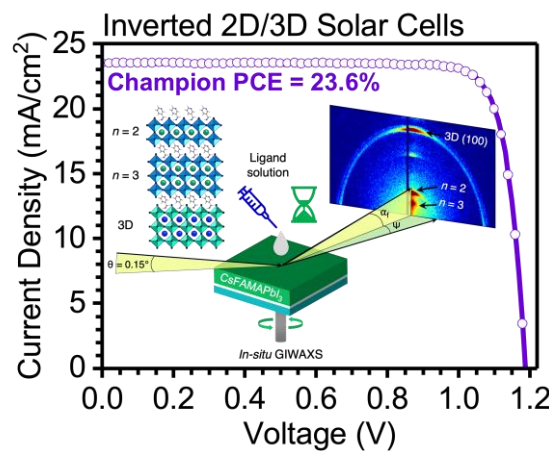
Table of Contents

This study elucidates the formation dynamics and film structure of 2D-Dion-Jacobson phase on a template of 3D triple-cation perovskite films via *in-situ* X-ray scattering. The solvent-induced surface reconstruction of the template allows the control of phase and phase distribution in 2D films. The tailored energy landscape of 2D/3D heterostructures leads to highly efficient and stable inverted perovskite solar cells.

Perovskite Solar Cells

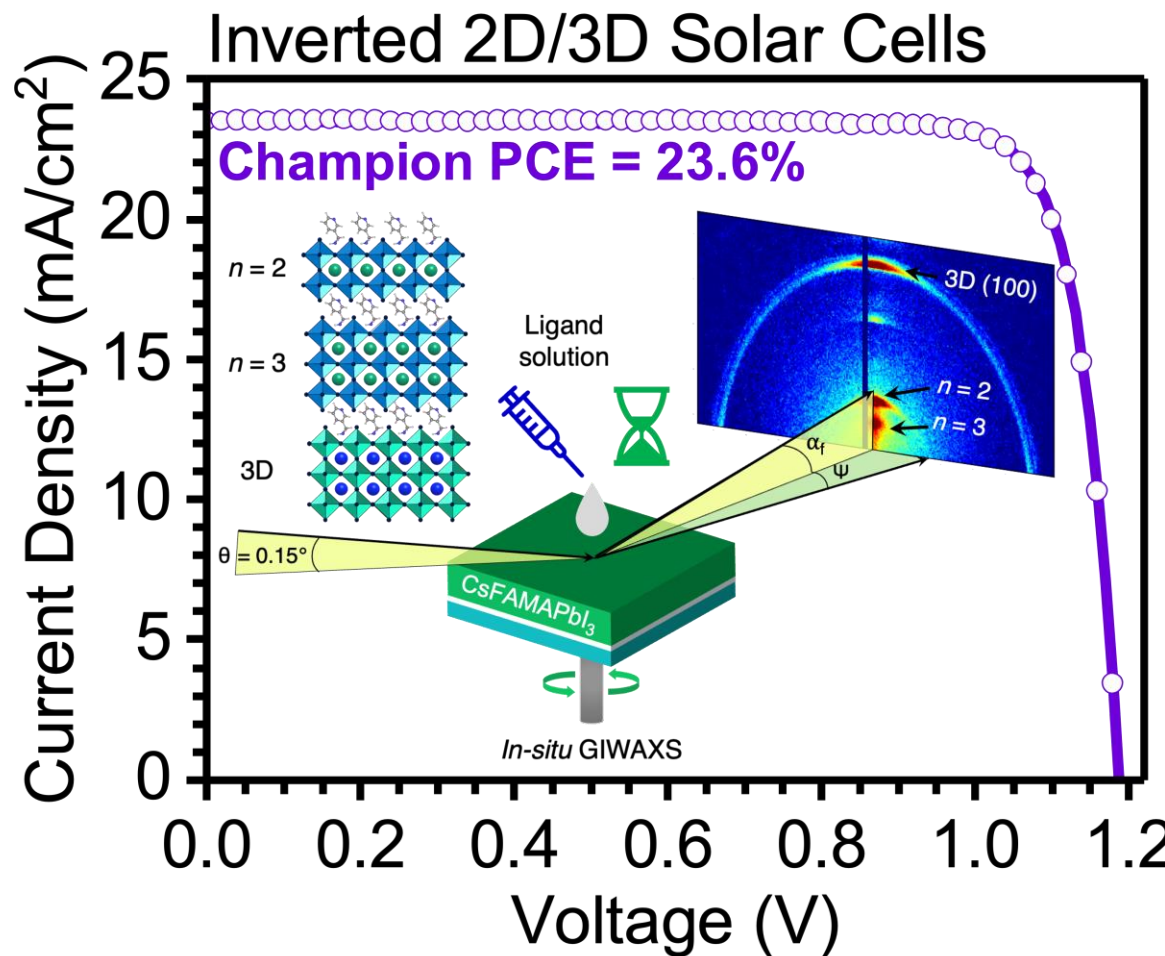
S. Ramakrishnan, D. Song, Y. Xu, X. Zhang, G. Aksoy, M. Cotlet, M. Li, Y. Zhang, and Q. Yu*

Solvent-Mediated Formation of Quasi-2D Dion-Jacobson Phases on 3D Perovskites for Inverted Solar Cells over 23% Efficiency



Solvent-Mediated Formation of Quasi-2D Dion-Jacobson on 3D Perovskite Heterostructures for Inverted Solar Cells over 23% Efficiency

Shripathi Ramakrishnan, Donghoon Song, Yuanze Xu, **Xiaoyu Zhang**, Gavin Aksoy, Mircea Cotlet, Mingxing Li, Yugang Zhang, Ruipeng Li, Honghu Zhang and Qiuming Yu*



Final word count: 60. Limit: 60.

This study elucidates the formation dynamics and film structure of 2D-Dion-Jacobson phase on a template of 3D triple cation perovskite films via *in-situ* X-ray scattering. The solvent-induced surface reconstruction of the template allows the control of phase and phase distribution in 2D films. The tailored energy landscape of 2D/3D heterostructures leads to highly efficient and stable inverted perovskite solar cells.